Faraday instability of binary miscible/immiscible fluids with phase field approach

M. Bestehorn,[1] D. Sharma,[2] R. Borcia,[1] and S. Amiroudine[2,*]
[1]*Institute of Physics, Brandenburg University of Technology, 03044 Cottbus, Germany*
[2]*Université Bordeaux, I2M UMR Centre National de la Recherche Scientifique 5295, Talence F-33400, France*

(Received 8 December 2020; accepted 18 May 2021; published 14 June 2021)

The objective in the present paper is to study binary fluids with phase field modeling coupled with Navier-Stokes equations. An extended free energy is proposed to account for the continuous path from immiscible to miscible states. We consider fluid pairs that are immiscible for temperatures below the critical one (consolute temperature) and miscible above it. Our extended phase field equation permits us to move from the immiscible state (governed by the Cahn-Hilliard equation) to the miscible state (defined by the species diffusion equation). The scaling of interface tension and interface width with the distance to the critical point is highlighted. The whole system is mechanically excited showing Faraday instability of a flat interface. A linear stability analysis is performed for the stable case (interface waves) as well as for the unstable Faraday one. For the latter, a Floquet analysis shows the well-known Arnold's tongues as a function of the consolute temperature and depth layer. Moreover, two-dimensional finite difference simulations have been performed allowing us to model nonlinear flow patterns both in miscible and immiscible phases. Linear theory and nonlinear simulations show interesting results such as the diminishing of the wavelength of Faraday waves or a shift of the critical vibration amplitude when the consolute temperature is approached.

DOI: 10.1103/PhysRevFluids.6.064002

I. INTRODUCTION

Faraday instability occurs when two fluid layers of different densities are parametrically excited with the imposed frequency in resonance with the system's natural frequency. The natural frequency depends on several parameters such as density difference, interfacial tension, viscosities, and geometry. Consequently, this parametric instability in the direction normal to the interface is commonly termed "Faraday instability". While immiscible fluid systems have been intensively studied in the literature, the case of miscible liquids, which is important to understand, for example in the mixing process, has not received significant attention. For liquid systems with low interfacial tension, gravitational force dominates the oscillatory convection and prevents gaining of insights into the phenomenon of capillary force. It thus requires a gravity-free environment in order to draw the different scenarios of instability with regard to these forces.

The motivation to study Faraday waves arises from several potential applications. One of the direct applications is the extrication of droplets and air formation in capillary tubes during space enabling operations. The generated waves are also widely utilized for fluid prototypes in order to produce microscale materials such as cell spheroids and cell-seeded microcarriers [1]. Faraday waves are also prevalent in natural phenomena such as in the intensification of seismic activity

*sakir.amiroudine@u-bordeaux.fr

through slacker sediments, while in the field of quantum mechanics, Faraday waves have been observed in Bose-Einstein condensates [2].

The phenomenon of the appearance of the remarkable array generated on a liquid surface near a vibrating surface was first reported by Oersted in 1813, Wheatstone in 1825, and Weber in 1825. Faraday [3] was the first to report the phenomenon in detail and deduced that the frequency of excited waves is half of the applied frequency. Mathematically, the parametric oscillation was first treated as a general phenomenon by Rayleigh [4,5]. He presented the argument for the existence of subharmonic solution. The first clear and complete theoretical description of the phenomenon was given by Benjamin and Ursell [6] who considered the instability in the inviscid limit. They condensed the linearized inviscid fluid equations of motion in the classical form of a Mathieu equation which is similar to parametric excitation of a linear harmonic oscillator.

Subsequent to inviscid hydrodynamic stability analysis by Benjamin and Ursell [6], Kumar and Tuckerman [7] presented the stability of a bilayer subjected to parametric vibration, including viscous effects in the Navier-Stokes equations. They performed a linear stability analysis for two laterally infinite layers of immiscible fluids with a Fourier-Floquet analysis for the disturbed interfacial deflection. Marginal stability curves for critical amplitude (threshold value) as a function of wave number were obtained. In the long wave approximation, reduced models have been derived by Bestehorn [8] for single-layer fluids and by Bestehorn and Pototsky for two-layer fluids [9]. These models were numerically verified by Richter and Bestehorn [10] by solving the full Navier-Stokes equations.

While immiscible fluid systems have been intensively studied in the literature as described above, the case of miscible liquids has not received significant attention. In miscible fluid systems, the interface is diffused at the start of mixing (in contrast to a sharp interface in an immiscible system) thus creating a gradient of density driving the instability. The instability grows with forced vibration and ultimately destroys itself with the mixing of the liquids. Zoueshtiagh *et al.* [11], Amiroudine *et al.* [12], and Diwakar *et al.* [13] presented results of experimental, numerical, and theoretical models with good qualitative and quantitative agreements. They described the importance of the waiting period before the vibration is set. As the waiting time is increased, diffusion in the system weakens the driving potential and results in smaller wavelengths. One of the key observations in these studies of miscible fluid systems is that they obtained similar dispersion relations as in [7] for immiscible fluid systems. It was considered that the reasons of growth of instability are similar to that of the immiscible case even if the factors leading to stabilization differ.

The question which has not been addressed thoroughly until now is the evolution of the instability in terms of modes when a two-fluid system evolves continuously from an immiscible state to a miscible one. Such fluids defined as binary fluids pose a very unique property of being soluble in each other depending on the temperature and are completely miscible above a certain temperature, called the consolute temperature or the critical temperature. The surface tension between the two fluids tends to zero and the interface thickness diverges as the consolute temperature is approached from below. Analyzing such a system requires the following two conditions to be satisfied. Firstly, the consolute temperature must be below the boiling temperature of both the fluids. Secondly, the interface must glide across the container wall thereby representing a minimization of the associated sidewall stresses or any disturbance generated by wall effects (periodic conditions in the analytical approach). In order to fulfill these conditions, a binary fluid system consisting of perfluorohexane (FC-72), a dense and inert fluorinated hydrocarbon, and octamethyltrisiloxane (1.0 cS silicone oil) can been chosen which produces an interface with very small negligible meniscus [14]. Low surface tension (less than 3 dyn/cm corresponding to the experimental value) was observed to be useful in reducing the sidewall stresses with a minimum meniscus and an almost not pinned triple contact line at the walls. Silicone oil also forms a tiny film on sidewalls around FC-72, making the interface floating almost stress free. The fluid consolute temperature is $\simeq$42.5 °C which is well below the boiling temperature of the more volatile (FC-72) component with boiling temperature of 56 °C.

The primary purpose of the present work is to study the evolution of the interface from an immiscible fluid system to a miscible one (in a discrete manner as the critical point is singular)

in order to pinpoint the effect of external vibration on wavelength when approaching the consolute temperature. This is performed by a phase field approach. The advantage of using the phase field approach is its inherent principle to consider the interface region as a diffused region which is similar to what we expect when we approach the critical temperature. An exact repeatability carries a demanding task in experimentations (by emptying and again filling the cell). The initial conditions (immiscible system at start) could be the same for different parameters (frequency and amplitude of vibration). By just increasing the temperature until the consolute temperature, we could bring the system to the desired miscible state. In order to bring back the system to the same initial immiscible state, it suffices to decrease the temperature and repeat the experiment for other vibration parameters.

II. PHASE FIELD APPROACH FOR THE PATH FROM IMMISCIBLE TO MISCIBLE STATES

In the phase field method, the interface is described as a region of smooth transition of properties from one fluid (or phase) to another. The idea was developed by Cahn and Hilliard [15,16] wherein an expression for the total free energy of the inhomogeneous system was derived taking into account the effects of local energy at the interface arising due to the gradient of concentration. The starting point of the phase field method thus lies in identifying the system to be inhomogeneous with respect to a certain intensive variable, termed the phase field variable (φ) followed by describing the total free energy including the gradient terms. Among several possible states for which the system could exist, the interface will move along the path toward minimizing the free energy for which a nonlinear partial differential equation, well known in the literature as the Cahn-Hilliard equation, was developed. The phase field equation is coupled to the momentum conservation in the Navier-Stokes equation by defining the surface tension forces as the interface energy per unit area. The coupled analysis of phase field with hydrodynamics, i.e., Navier-Stokes–Cahn-Hilliard, was undertaken by Gurtin *et al.* [17] following which several pioneering works [18–21] have led to a noteworthy advancement of the subject [22–25].

A. Cahn-Hilliard equation

As a starting point, we use an extension of the Cahn-Hillard equation [15,16] derived from the variation of a free energy functional with respect to a real-valued phase field φ (see also Jacqmin [26] and Ding *et al.* [27]). Herein we propose a modified free energy functional which can be written as

$$F[\varphi] = \frac{1}{2}\int_V \left[K\theta(r)r^p|\nabla\varphi|^2 - r_0 r\varphi^2 + \frac{1}{2}r_0\theta(r)r^q\varphi^4\right]dV, \tag{1}$$

where K and r_0 are related to surface tension and interface thickness, $\theta(r)$ denotes the Heaviside function, and r is a control parameter vanishing at the consolute temperature. Taking $r = 1$ as a reference point well below the critical temperature (immiscible state), one finds for the interface width [3] $\zeta_0 = \sqrt{K/r_0}$, and for the surface tension $\sigma_0 = \frac{2}{3}\sqrt{2Kr_0}$ (see details in Appendix A). For example, for $\zeta_0 = 10^{-8}$ m and $\sigma_0 = 0.014$ N/m, $K = 1.5\ \ 10^{-10}$ N and $r_0 = 1.5\ \ 10^6$ N/m^2.

As will be shown in Sec. II C, the two positive exponents p and q can be adjusted to the experimentally observed behavior of surface tension, interface thickness, and mixing ratio when the critical point is approached ($r \to 0^+$). Here, for $r = 1$, the original Cahn-Hilliard equation is recovered. The key parameter in this sudy is the nondimensional parameter r allowing to model the phase transition from the miscible state ($r < 0$) to the immiscible one ($r > 0$); see Fig. 1. Further details and developments on this parameter will be described later. The advected form of the Cahn-Hillard equation can be written as (see [15,16])

$$\frac{d\varphi}{dt} = \nabla\cdot[M\nabla\mu]. \tag{2}$$

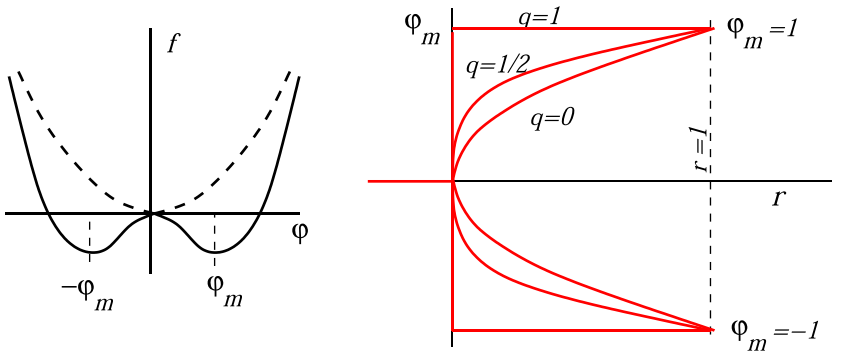

FIG. 1. Left: sketch of the bulk potential free energy $f = -\frac{1}{2}r_0 r\varphi^2 + \frac{1}{4}r_0\theta(r)r^q\varphi^4$ in the miscible phase $r < 0$ (dashed), and in the immiscible phase $r > 0$ (solid). Right: phase field in the bulk as a function of r for different values of q ($\varphi_m = \pm r^{\frac{1-q}{2}}$ corresponds to the minimum values of the phase field for the two fluid components, for $r > 0$).

Here and in the following, $d/dt = \partial_t + \vec{V}\cdot\nabla$ denotes the material derivative with $\vec{V}$ representing the velocity vector, M is the mobility parameter, and μ the extended chemical potential given by (see also the orginal expression in [28])

$$\mu = \frac{\delta F}{\delta \varphi} = -K\theta(r)r^p\Delta\varphi - r_0 r\varphi + r_0\theta(r)r^q\varphi^3. \tag{3}$$

Let the system have the depth d (see Fig. 2) and kinematic viscosity ν (for sake of simplicity, we assume the same value for both components). Scaling all lengths with d and time with $\tau = d^2/\nu$ (the notation of dimensionless variables is kept the same henceforth), Eq. (3) leads to

$$\frac{d\varphi}{dt} = \tilde{M}\Delta[-\tilde{K}\theta(r)r^p\Delta\varphi - r\varphi + \theta(r)r^q\varphi^3], \tag{4}$$

with $\tilde{M} = Mr_0/\nu$ and $\tilde{K} = K/(r_0 d^2)$. Here and for the following we assume M and K are independent from the phase field variable and are held constant. For $\tilde{M} = 1$, we have $M = \nu/r_0$.

B. Navier-Stokes equations and the corresponding complete model

A two-dimensional (2D) incompressible fluid coupled to the phase field is defined by the following dimensional Navier-Stokes equations (the same notation of dimensional and nondimensional variables will be used subsequently):

$$\rho\frac{d\vec{V}}{dt} = -\nabla P + \eta\Delta\vec{V} + \mu\nabla\varphi - \rho g\vec{e}_y, \tag{5}$$

$$\nabla\cdot\vec{V} = 0, \tag{6}$$

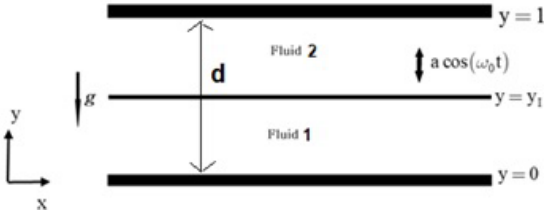

FIG. 2. Sketch of the geometry of the two-fluid layer.

where P is the pressure field, η is the dynamic viscosity, and the term $\mu\nabla\varphi$ represents the surface tension term, implicitily representing the Korteweg stress [24].

In order to eliminate the pressure in Eq. (5), we introduce the stream function ψ by $V_x = \partial_y\psi$, $V_y = -\partial_x\psi$ and Eq. (5) reduces thus to

$$\frac{d\Delta\psi}{dt} = \Delta^2\psi + G\partial_x\left(\frac{\rho}{\rho_0}\right) - \Gamma\theta(r)r^p(\partial_y\Delta\varphi\partial_x\varphi - \partial_x\Delta\varphi\partial_y\varphi), \tag{7}$$

where Δ^2 is the biharmonic operator and

$$G = \frac{gd^3}{\nu^2}, \quad \Gamma = \frac{K}{\nu^2\rho_0} = \frac{3}{2\sqrt{2}}\ \frac{\sigma_0\zeta_0 d}{\nu^2\rho_0}. \tag{8}$$

G and Γ are the Galileo and the inverse capillary numbers, respectively. Note that ζ_0 is now dimensionless with respect to d. The coupling from the phase field to the stream function is due to normal and tangential forces at the interface (Korteweg stress [28]) and buoyancy.

Instead of considering the Lagrangian time derivative of the density for the mass conservation equation [Eq. (6)] (Lowengrub and Truskinovsky [29]), the Boussinesq approximation has been applied, assuming $\rho = \rho_0$ is constant everywhere [Eqs. (5) and (6)] except in the buoyancy term, where it depends on φ. In order to close the system, an equation of state of the form $\rho = \rho(\varphi)$ is required which is approximated here as a linear function, $\rho = \rho_0[1 + \delta\rho(\varphi + 1)]$ with $\delta\rho = \frac{\rho_1 - \rho_0}{2\rho_0}$, ρ_1 being the density for fluid 1 represented by $\varphi = 1$ and ρ_0 for fluid 2 with $\varphi = -1$ (see Fig. 2). It is worth mentioning here that, in the Boussinesq approximation we do not consider density variations in the continuity equation [Eq. (6)] and we therefore neglect terms of $0(\delta\rho)$ in which $\delta\rho$ is small. Our analysis is thus limited to cases where the density of the two components is of the same order as also considered by Takagi and Matsumoto [30].

One of the major problems in phase field theory is that the physical width of the interface (which is of the order of a few nanometers) is much smaller than the size of the cell and the wavelength of the obtained patterns (some millimeters). We thus define the "numerical width" $\zeta_N = s\zeta_0$ which is obtained from Eq. (4) by renormalizing $K_N = s^2K$ and subsequently in Eq. (8), $\Gamma_N = \frac{K_N}{\nu^2\rho_0} = \frac{s^2K}{\nu^2\rho_0} = \frac{3}{2\sqrt{2}}\frac{s\sigma_0\zeta_N d}{\nu^2\rho_0}$.

However, due to the larger interface width, the surface tension reflected by this Γ_N also increases by a factor of s. We thus renormalize Γ_N by s and define $\bar{\Gamma}_N = \frac{3}{2\sqrt{2}}\frac{\sigma_0\zeta_N d}{\nu^2\rho_0}$ which will be used in the following numerical computations.

The complete scaled version of the model can thus be written as

$$\frac{d\Delta\psi}{dt} = \Delta^2\psi + \delta\rho G\,\partial_x\varphi - \bar{\Gamma}_N\theta(r)r^p(\partial_y\Delta\varphi\partial_x\varphi - \partial_x\Delta\varphi\partial_y\varphi), \tag{9}$$

$$\frac{d\varphi}{dt} = \Delta[-K_N\theta(r)r^p\Delta\varphi - r\varphi + \theta(r)r^q\varphi^3]. \tag{10}$$

Note that for $r = 1$ the dimensionless width ζ_N is related to K_N via $\zeta_N^2 = K_N$.

The set of Eqs. (9) and (10) is complemented by the no-slip conditions for ψ, which can be written as

$$\psi = \partial_y\psi = 0 \ \text{ at } \ y = 0, 1. \tag{11}$$

The conditions of impermeable walls and therefore the vanishing mass flux through the boundaries yield one boundary condition for μ:

$$\partial_y\mu = 0. \tag{12}$$

Using, Eq. (3), Eq. (12) can be written in terms of φ as

$$\partial_y\varphi = \partial^3_{yyy}\varphi = 0 \ \text{ at } \ y = 0, 1. \tag{13}$$

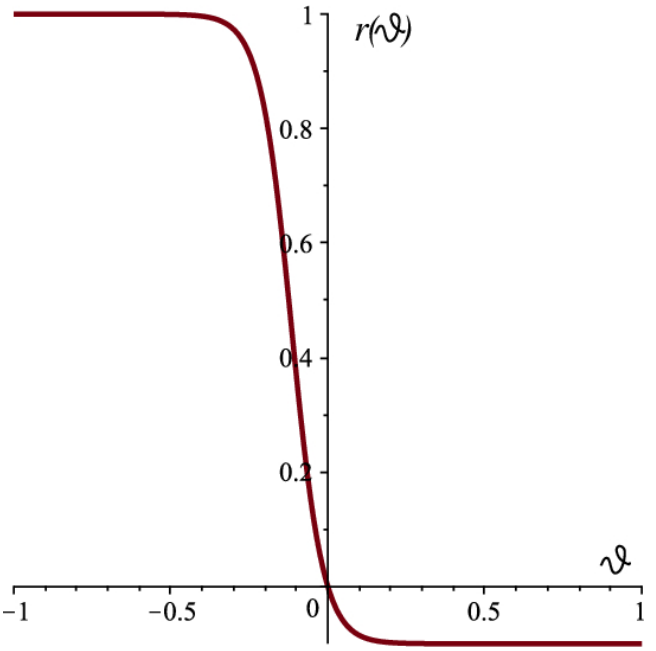

FIG. 3. Function $r(\vartheta)$ for $a = 10$ and $\mathrm{Sc} = 10$.

The choice in Eq. (13) is not unique and one could also use Eq. (12) as one condition along with a relation between φ, $\partial_y\varphi$ with the contact angle (wetting property of the walls). Our current choice fixes the contact angle of drops for both liquids at the walls as 90 ° (see Fig. 9 below). A detailed discussion on boundary conditions on surfaces where concentration affects the wetting conditions can be found in Thiele *et al.* [31].

C. Critical exponents

Our extended Cahn-Hilliard equation is constructed in such a way that below the critical temperature, the two fluids are immiscible and Eqs. (9) and (10) are solved (Navier-Stokes with extended phase field equations); on the other hand, above the critical temperature, there is no interface and Eq. (10) is transformed into a concentration equation of species with a vanishing Korteweg term in Eq. (9); i.e.,

$$\frac{d\Delta\psi}{dt} = \Delta^2\psi + \delta\rho G\,\partial_x\varphi, \tag{14}$$

$$\frac{d\varphi}{dt} = -r\Delta\varphi. \tag{15}$$

For this case the boundary conditions in Eq. (12) reduce to the no-diffusive flux condition given by $\partial_y\varphi = 0$ at $y = 0,\ 1$. In order to study these conditions, r is defined as $r = r(\vartheta)$, $r(0) = 0$, $\frac{dr}{d\vartheta} < 0$ with the reduced temperature $\vartheta = \frac{T-T_c}{T_c}$. In order to cover the asymptotic behavior below and above the critical temperature, the following constraints must hold: $r(\vartheta \ll 0) = 1$, $r(\vartheta \gg 0) = -1/\mathrm{Sc}$, where $\mathrm{Sc} = \nu/D$ is the Schmidt number and D is the mass diffusion coefficient. A possible "r" function that could be used is the following: $r(\vartheta) = \frac{e^{-a\vartheta} - e^{a\vartheta}}{e^{-a\vartheta} + S_c e^{a\vartheta}}$ with $a > 0$ (the factor a can be determined from the variation of the temperature in experiments). Figure 3 shows the evolution of the parameter r as a function of ϑ for $a = 10$ and $\mathrm{Sc} = 10$. As can be seen in this figure, the asymptotes $r = 1$, $r = -1/\mathrm{Sc}$ are reached for $\vartheta \to \pm\infty$.

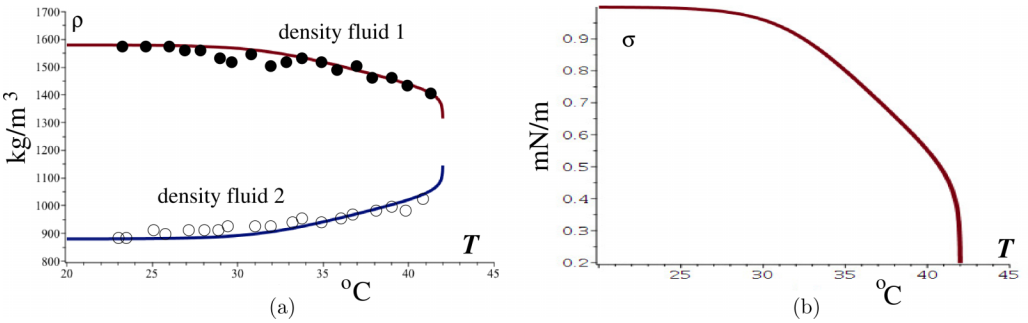

FIG. 4. (a) Densities of the two phases (solid lines) adjusted to experimental data (circles) by chosing values for a, Sc, and q [32]; (b) surface tension as a function of T for the same parameters and $p = 1/7$.

Computing the r-dependent surface tension and interface width from Eq. (9) yields, for $r > 0$,

$$\sigma(r) = \sigma_0 r^{\alpha}, \quad \zeta(r) = \zeta_0 r^{\beta}, \tag{16}$$

with the exponents $\alpha = \frac{p+3}{2} - q$, $\beta = \frac{p-1}{2}$ (see Appendix A). These exponents can be adjusted to experimental data or microscopic theories. Here, $\zeta_0 = \zeta(1) = \sqrt{K/r_0}$ and $\sigma_0 = \sigma(1) = \frac{2}{3}\sqrt{2Kr_0}$.

For $r \to 0^+$, one expects $\zeta \to \infty$, $\sigma \to 0$ leading to the conditions $\alpha > 0$, $\beta < 0$, or $p < 1$, $q < \frac{p+3}{2}$. Further, the parameter q can be used to adjust the bulk density behavior $\rho(\varphi_m)$ with $\varphi_m = \pm r^{\frac{1-q}{2}}$ as a function of the temperature to experimental data [32]. Figure 4(a) shows the situation for $a = 10$, $T_c \approx 42\,^{\circ}\mathrm{C}$, $\mathrm{Sc} = 100$, $q = 3/4$ and the two asymptotic densities $\rho_o = 880\,kg/m^3$ (silicone oil), $\rho_1 = 1580\ \mathrm{kg/m^3}$ (FC72), ($\delta\rho = 0.39$). In the same way, surface tension (no experimental data are available for this set of fluids) as a function of T is found wherein we have used $p = 1/7$ in Fig. 4(b). This value of $p = 1/7$ is justified by the fact that the surface tension smoothly decreases as a function of temperature in order to reach a zero value at the consolute temperature defined for the given set of fluids (silicon oil, FC72).

III. LINEAR STABILITY ANALYSIS BELOW THE CRITICAL TEMPERATURE

A linear stability analysis of a phase field model coupled to hydrodynamics was performed earlier in [33,34] for a free surface and Marangoni convection. Here we shall consider the stability of our extended model [Eqs. (9) and (10)], firstly for the undriven case followed by a periodically modulated gravity force (Faraday instability). Since no stationary inhomogeneous state exists in the miscible regime, we will limit our study to the immiscible case $r > 0$ for the stability analysis. A gravitationally stable solution of Eqs. (9) and (10) for $\delta\rho > 0$ is given by the stationary state:

$$\psi_0 = 0, \quad \varphi_0(y) = -r^{\frac{1-q}{2}} \tanh\left[\frac{y - 1/2}{\sqrt{2\tilde{K}_N}} r^{\frac{1-p}{2}}\right], \tag{17}$$

where the lighter fluid is positioned on top of the heavier one. Linearization of Eqs. (9) and (10) according to $\varphi(x, y, t) = \varphi_0(y) + \hat{\phi}(y)\, e^{\,ikx+\lambda t}$, $\psi(x, y, t) = \hat{\psi}(y)\, e^{\,ikx+\lambda t}$ yields the following linear ordinary system (primes denote derivatives with respect to y):

$$\lambda\hat{w} = \hat{w}'' - k^2\hat{w} + ik\delta\rho G\hat{\phi} - ik\bar{\Gamma}_N r^p[(\varphi'''_0 + k^2\varphi'_0)\hat{\phi} - \varphi'_0\hat{\phi}''], \tag{18}$$

$$\begin{aligned}\lambda\hat{\phi} = {} & -\tilde{K}_N r^p(k^4\hat{\phi} - 2k^2\hat{\phi}'' + \hat{\phi}'''') + r(k^2\hat{\phi} - \hat{\phi}''), \\ & + 3r^q\left[\left(2\varphi_0\varphi''_0 2\varphi_0^{2\prime} - \varphi_0^2k^2\right)\hat{\phi} + 4\varphi_0\varphi'_0\hat{\phi}' + \varphi_0^2\hat{\phi}''\right] + ik\varphi'_0\hat{\psi},\end{aligned} \tag{19}$$

with an auxilary vorticity function defined by

$$\hat{w} = \hat{\psi}'' - k^2 \hat{\psi}. \tag{20}$$

The system of Eqs. (18)–(20) will be studied numerically in the following section.

A. Formulation as an algebraic eigenvalue problem

We apply finite differences for the y derivatives of order Δy^2, with the following discretization for $\hat{w}$, $\hat{w}_j = \hat{w}(y_j)$, $y_j = j\Delta y$, $j = 1 \cdots N$, $\Delta y = 1/(N+1)$, and the same for $\hat{\phi}$ and $\hat{\psi}$ with N representing the number of mesh points. Then the set of Eqs. (18)–(20) is transformed to an algebraic system of equations:

$$\lambda \ \vec{Q} = \underline{M} \ \vec{Q}, \tag{21}$$

where $\underline{M}$ is a real-valued $2N \times 2N$ matrix and the vector $\vec{Q}$ comprises the unknown variables:

$$Q_j = i\hat{w}_j, \quad Q_{N+j} = \hat{\phi}_j, \quad j = 1 \cdots N,$$

(here, i stands for $\sqrt{-1}$). The N variables $\hat{\psi}_l$ are eliminated by discretizing Eq. (20):

$$\hat{\psi}_l = \sum_j^N A^{-1}_{lj} \hat{w}_j, \quad j = 1 \cdots N, \tag{22}$$

where $\underline{A}^{-1}$ is the inverse of a $N \times N$ tridiagonal matrix of the following form:

$$A_{ll} = -2/\Delta y^2 - k^2, \quad A_{l,l+1} = A_{l,l-1} = 1/\Delta y^2. \tag{23}$$

The elements of $\underline{M}$ are listed in Appendix C. From Eq. (22), the N inner nodes of $\hat{\psi}$ are determined. The values for $\hat{\psi}_0$ and $\hat{\psi}_{N+1}$ must be zero due to the no-slip condition $V_x = V_y = 0$ which implies $\hat{\psi} = \hat{\psi}' = 0$ at $y = 0,\ 1$. The second condition, $\hat{\psi}' = 0$, is transformed into the conditions needed for w and reads (for details, see [35,36])

$$\hat{w}_0 = \frac{2\hat{\psi}_1}{\Delta y^2}, \quad \hat{w}_{N+1} = \frac{2\hat{\psi}_N}{\Delta y^2}.$$

The analytical solution [Eq. (17)] differs by the discretization error from a numerically computed stationary solution of Eq. (10). Taking Eq. (17) as the base state yields a small but positive growth rate. Thus, it is consistent to compute the stationary base state numerically with the same finite differences discretization used to obtain Eq. (21); this base state φ_0 is then numerically stable and computed iteratively by solving the discretized form of Eq. (10),

$$0 = r\varphi_{0j} + K_N r^p \frac{\varphi_{0j+1} - 2\varphi_{0j} + \varphi_{0j-1}}{\Delta y^2} - r^q \varphi_{0j}^3, \tag{24}$$

until a completely steady solution is found. From there, the derivatives of φ_0 are computed using finite differences again.

The boundary conditions (at $y = 0,\ 1$) applied in Eqs. (19) and (24) are

$$\hat{\phi} = \hat{\phi}' = 0, \quad \varphi_0 = \pm r^{\frac{1-q}{2}}. \tag{25}$$

For simplicity we may use here Eq. (25) instead of Eq. (13) since the instability occurs at the edge of the front around $y = 1/2$. Note also that the solution of Eq. (17) satisfies Eq. (25) up to an accuracy of $\sim \exp(-48)$ for the smallest $r = 0.1$ used in the current work.

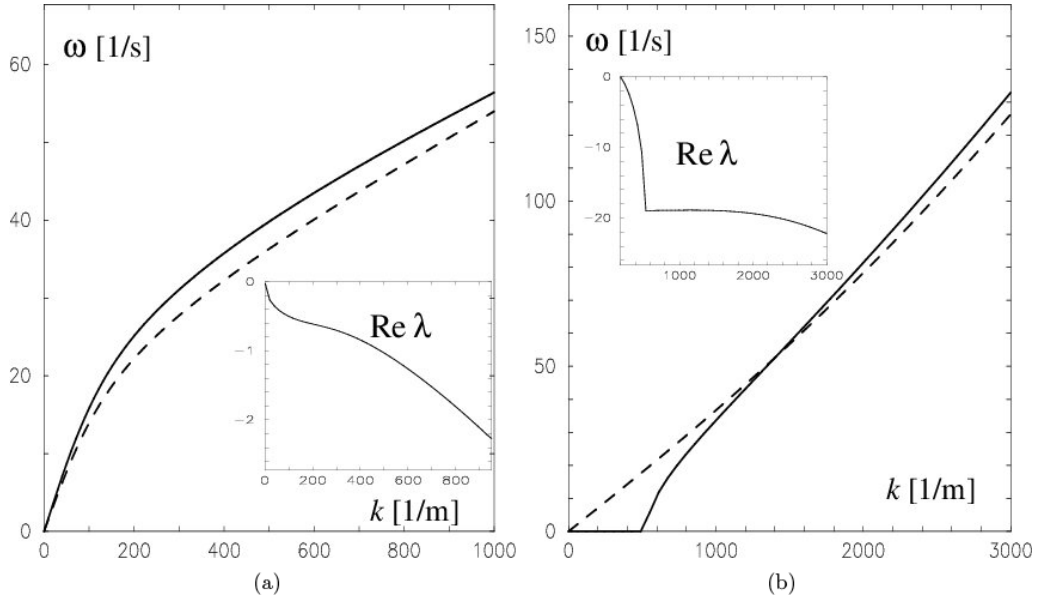

FIG. 5. Frequency of the least stable modes (largest real part) over k for $r = 1$. Parameters: At $= 0.26$, $\sigma = 0.001$ N/m, $\rho_0 = 10^3$ kg/m^3, $\nu = 10^{-6}$ m^2/s; (a): $d = 1$ cm, (b): $d = 1$ mm. The dashed lines show the exact results for an inviscid liquid, Eq. (26). The insets show the eigenvalues with the largest real part for the viscous case computed by our analysis. In (b), a real-valued eigenvalue crosses a complex one at $k \approx 500$/m.

B. Dispersion relation of interface waves: The unforced system

We first show results for $N = 400$ and $K_N = 0.7 \times 10^{-4}$, corresponding to an interface width of $\zeta_N \approx 0.0084$. Thus the interface is resolved with up to three to four mesh points. A two-fluid system (with properties close to the binary mixture, FC72-silicone oil) has been considered in this study in order to see the effect of transition from immiscible to miscible states with the following physical parameters, $\nu = 10^{-6}\,\mathrm{m}^2/\mathrm{s}$, $\rho_0 = 10^3\,\mathrm{kg/m}^3$, $\sigma_0 = 0.001\,\mathrm{N/m}$, $\delta\rho = 0.35$, and $d = 1\,\mathrm{cm}$ which gives $G \approx 9.81 \times 10^6$, $\bar{\Gamma}_N \approx 89$.

In Fig. 5, the frequencies $\omega = \mathrm{Im}\,(\lambda)$ are shown for the eigenvalue with the largest real part. The results are compared with the analytical results for an inviscid layer (ω_I), given as ([37])

$$\omega_I = \sqrt{\left(\mathrm{At}gk + \frac{\sigma_0 k^3}{\rho_0 + \rho_1}\right)\tanh\,(kd/2)}, \tag{26}$$

with the Atwood number, $At = \frac{\rho_1 - \rho_0}{\rho_1 + \rho_0} = \frac{\delta\rho}{\delta\rho + 1}$.

In order to see the effect of depth (which is related to the effect of viscosity), two cases have been computed: $d = 1\,\mathrm{cm}$ and $d = 1\,\mathrm{mm}$. As the surface tension coefficient is very small for the case considered in this study, the second term in Eq. (26) is negligible at least for small values of k. For small values of k, $\tanh(kd/2) \approx kd/2$ and consequently $\omega \sim k$ (shallow water). For larger values of k, $\tanh(k\,d/2) \approx 1$ and $\omega \sim \sqrt{k}$. These two effects are clearly seen in Fig. 5. The agreement with the inviscid liquids is very good, especially for thicker layers in which the influence of viscosity is less important than in the case of thinner layers.

C. Faraday instability

A central point of the present paper is to submit an external force (vibration) to the two-fluid system described in the previous section. The originality of the present work is to set up Faraday

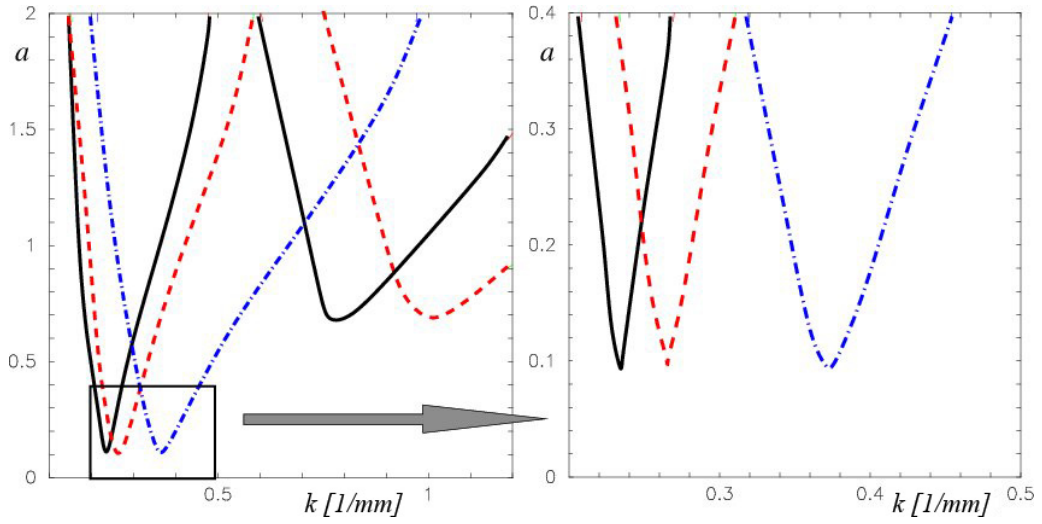

FIG. 6. Stability diagram of the Faraday instability for $\omega_0 = 50$ rad/s and with the same parameters as Fig. 5(a); solid line $r = 1$, dashed line $r = 0.5$, and dashed-dotted line $r = 0.1$.

instability from the immiscible system for which the temperature is below the critical temperature to the miscible system where the temperature is above the critical temperature. The goal is to analyze the evolution of Faraday instability during this transition. The main hypothesis in this system is to consider the temperature homogeneous so that the system of equations does not consider any energy equation.

The two-fluid system is harmonically vibrated in the vertical direction, leading to an effective gravity acceleration in the comoving frame of the form $g_e(t) = g[1 + a\cos(\omega_0 t)]$ with the two new control parameters a (dimensionless acceleration) and frequency ω_0. Consequently, the effective dimensionless gravity in Eq. (9) can be written as

$$G_e(t) = G\,[1 + a\cos(\omega_0 t)]. \tag{27}$$

The linear analysis now leads to a set of $2n$ ordinary differential equations (ODEs):

$$\frac{d\vec{Q}(t)}{dt} = \underline{M}(t)\vec{Q}(t), \tag{28}$$

with $\underline{M}(t)$ identical to the one in Eq. (21) except that G is replaced by $G_e(t)$.

Integrating numerically Eq. (28) for $2N$ orthonormal initial conditions (see details in Appendix D) with $Q_i^j(0) = \delta_{ij}$ over one period $T_0 = 2\pi/\omega_0$, the $2N \times 2N$ monodromy matrix $\underline{X}$ is found as $X_{ij} = Q_i^j(T_0)$. The real parts of the Floquet exponents are given as $\lambda_i = \frac{1}{T_0}\ln|\alpha_i|$, where α_i are the eigenvalues of $\underline{X}$. According to Floquet's theorem, $\lambda > 0$ denotes an instability of the flat surface. Plotting the zero lines of the largest λ_i in the (ak) plane yields the typical tongues shown in Figs. 6 and 8.

Figure 6 illustrates the stability diagram for the immiscible region with different values of r. Inside the tongues, the flat surface is unstable due to the Faraday instability. The tongues on the left belong to the subharmonic mode (the pattern oscillates with a frequency of $\omega_0/2$) and the right ones correspond to the harmonic branch. With decreasing r, the locations of the minima change, the wave number increases, and the wavelength thus decreases. This will be shown and highlighted in Sec. IV through direct numerical simulations (DNS) calculations. In addition, we observe that the minima do not change much with varying r. In order that the surface tension plays a role, the wavelength must be of the order of the capillary length, i.e., $\frac{2\pi}{k} \sim \sqrt{\frac{\sigma_0}{g\rho_0}} \simeq 0.3\,\text{mm}$, which gives $k \simeq 20\,\text{mm}^{-1}$.

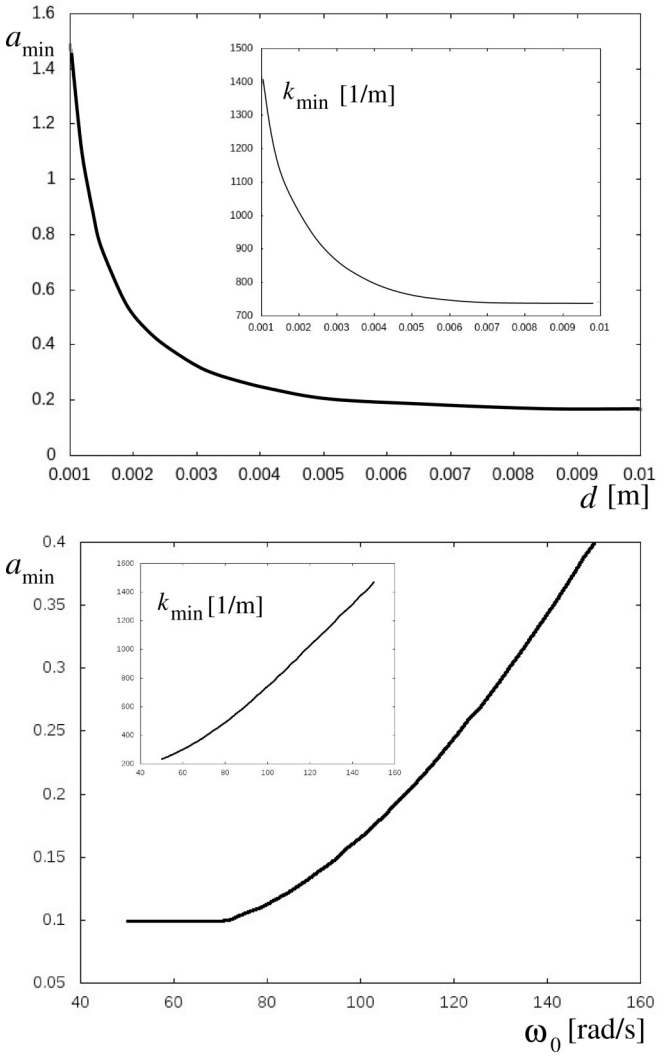

FIG. 7. Minimum values of acceleration for which the Faraday instability emerges with $k = k_{min}$ (insets). Top: as a function of the depth d for fixed frequency $\omega_0 = 100\,\mathrm{rad/s}$; bottom: as a function of ω_0 for fixed depth $d = 1\,\mathrm{cm}$. Same parameters as in Fig. 5.

This value is far from the values shown in Fig. 6 which proves that the effect of surface tension is indeed negligible in the range of our given parameters.

Figure 7 shows the theshold (minimum) value of the amplitude of acceleration a_{min} as a function of the depth d [Fig. 7(a)] and the frequency ω_0 for the same parameters as in Fig. 5(a). In the insets of these figures, the critical value of the wave number k_{min} is also shown as a function of d and ω_0. One can see that a_{min} and k_{min} both decrease with depth d and saturate at higher values of d due to the viscous damping. As d increases the system is more unstable. Moreover, as the frequency of the system is increased, the critical acceleration increases meaning that it is more and more stable which has also been observed experimentally by Zoueshtiagh *et al.* [11] (see Fig. 9 in their paper).

Figure 8 shows the stability diagram for a higher frequency than in Fig. 6 and different depths. The instability is shifted toward smaller wavelengths and larger critical acceleration if ω is increased or if d is decreased.

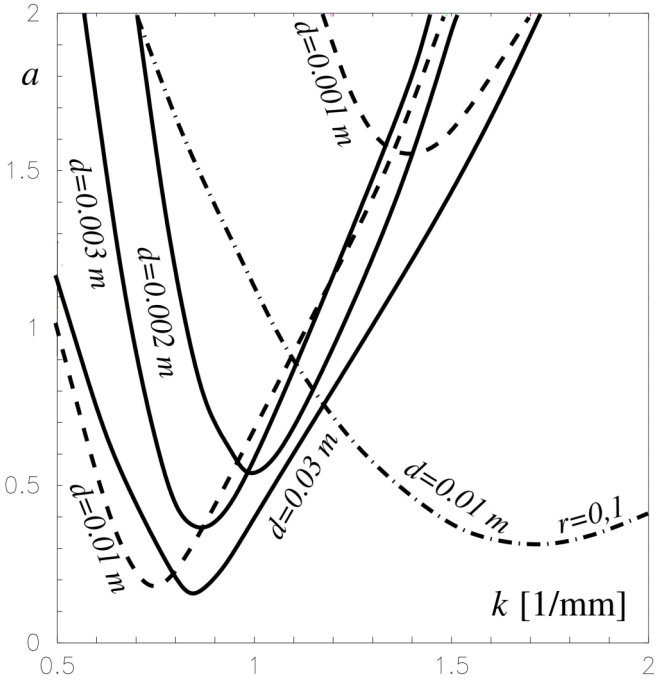

FIG. 8. First tongues for $\omega_0 = 100$ rad/s and several layer depths. All curves are for $r = 1$ except for the dashed-dotted one which is for $r = 0.1$.

IV. NUMERICAL RESULTS OF THE NONLINEAR SYSTEM

The analysis presented in the previous section provides a glimpse of the effect of changing the distance from the consolute temperature further motivating the exploration of the problem to gain insight into the physical behavior involved. We thus peform a numerical analysis of the full set of governing equations [Eqs. (9) and (10)] with the same physical parameters as defined in Sec. III B, i.e., $\nu = 10^{-6}\,\mathrm{m}^2/\mathrm{s}$, $\rho_0 = 10^3\,\mathrm{kg/m}^3$, $\sigma_0 = 0.001\,\mathrm{N/m}$, $\delta\rho = 0.35$ and $d = 1\,\mathrm{cm}$. The results are presented in the folowing sections. We applied a semi-implicit pseudospectral method where parts of the system are computed in lateral Fourier space. For the vertical direction, a finite difference method is applied (for details see Appendix B).

The primary objective of the current work is to model transition from a two-phase to a monophase region in incompressible fluids and analyze its effect on some canonical cases, i.e., Faraday and Rayleigh-Taylor instabilities. Further, we have refrained from carrying out any extensive parameter study and have only focused attention on certain distances (in terms of temperature) from the critical temperature and have thus considered r as the control parameter. We therefore assume the values $p = q = 1/2$ as explained above, leading to the exponents $\alpha = 5/4$, $\beta = -1/4$ for all the following analysis. Further, by taking $K_N = 0.7 \times 10^{-4}$, the dimensionless interface thickness is $\approx 0.84 \times 10^{-2}$. The dimensionless time step considered in all the simulations is in the range of $0.4-1.5 \times 10^{-6}$. Finally, for better visualization for the reader, we have provided the time series videos in the form of movies in the Supplemental Material [38] for the reader.

A. Phase separation in the unforced system of two fluids

All runs in this section have been initialized with a random-dot distribution of the phase field with vanishing mean, $\varphi(x, y, t = 0) = \xi(x, y)$, and equally distributed random numbers in $-0.1 < \xi < 0.1$. Below the critical point ($r > 0$) the heavier component sinks and accumulates in the lower

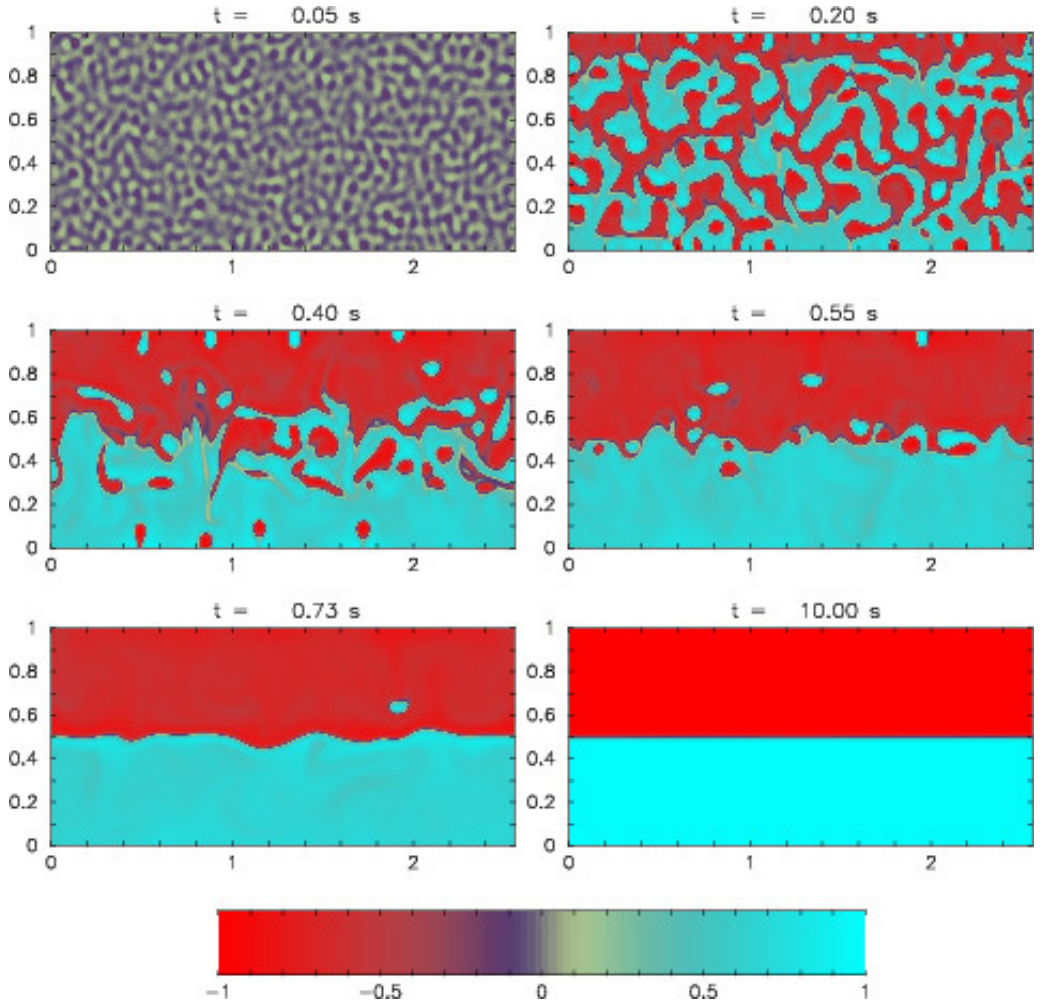

FIG. 9. Time series for $r = 1$; length is in cm. Different colors correspond to the values of the phase field. The FD mesh has the size 1024×400, corresponding to an aspect ratio of 2.56. See the movie in the Supplemental Material [38] for the time evolution of the phase field for the unforced system from a random-dot initial distribution of the phase field and below the critical temperature (immiscible state at $r = 1$).

half of the layer due to gravitation (Figs. 9 and 11). If the layer is turned upside down, the system is unstable with respect to the Rayleigh-Taylor instability. After a short time the two fluid layers exchange their positions and a gravitationally stable configuration is approached as a steady state solution (Fig. 10).

On comparing Figs. 9 and 11, one can see that as soon as the value of r diminishes (from 1 to 0.1, which means that the critical temperature is approached), the pattern formation is more and more diffusion dominated, while the role of convection is significantly reduced (see Fig. 11) and there still exists a clear diffused interface between the two fluids. One can also notice that the two fluids are more or less mixed during a long transient phase. Further, it is obvious that the time needed to finally establish a sharp interface increases with decreasing r. This is due to the fact that the typical evolution time scales with $1/Mr$ (critical slowing down). This is clearly shown in Figs. 9 and 11 in which it takes by a factor $1/r \approx 10$ longer until the sharp interface occurs. Our computations show that this can be compensated by adjusting the mobility by a factor of $1/r$ (not shown here).

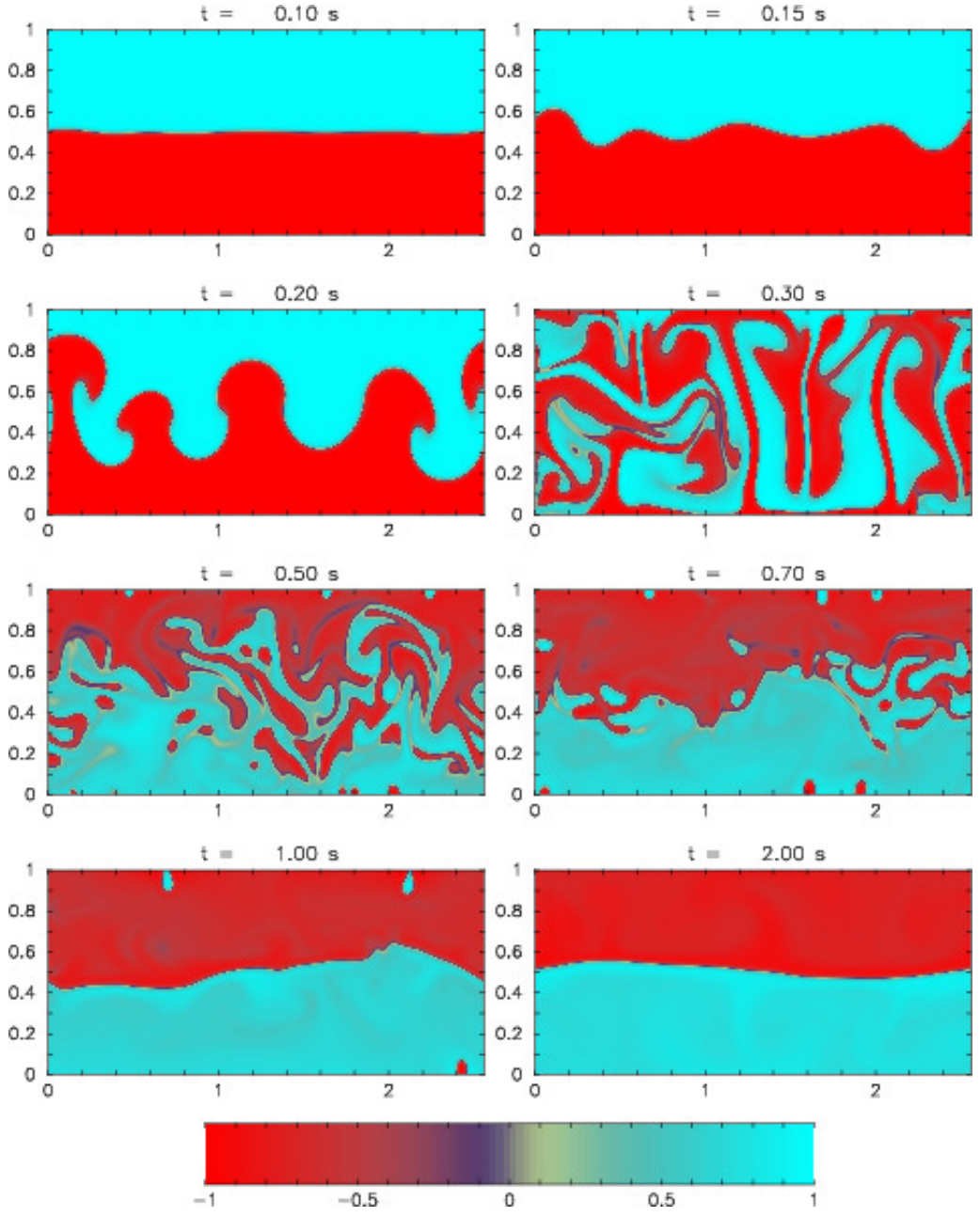

FIG. 10. Run for the initial condition from Fig. 9 last frame ($t = 10$s), but mirrored on the $y = 1/2$ plane. Now the heavier fluid is placed on top of the lighter one and the system is gravitationally unstable (Rayleigh-Taylor instability). All parameters are the same as in Fig. 9. See the movie in the Supplemental Material [38] for time evolution of the phase field in Rayleigh-Taylor configuration (heavier fluid placed above the lighter one) far from the critical temperature (at $r = 1$).

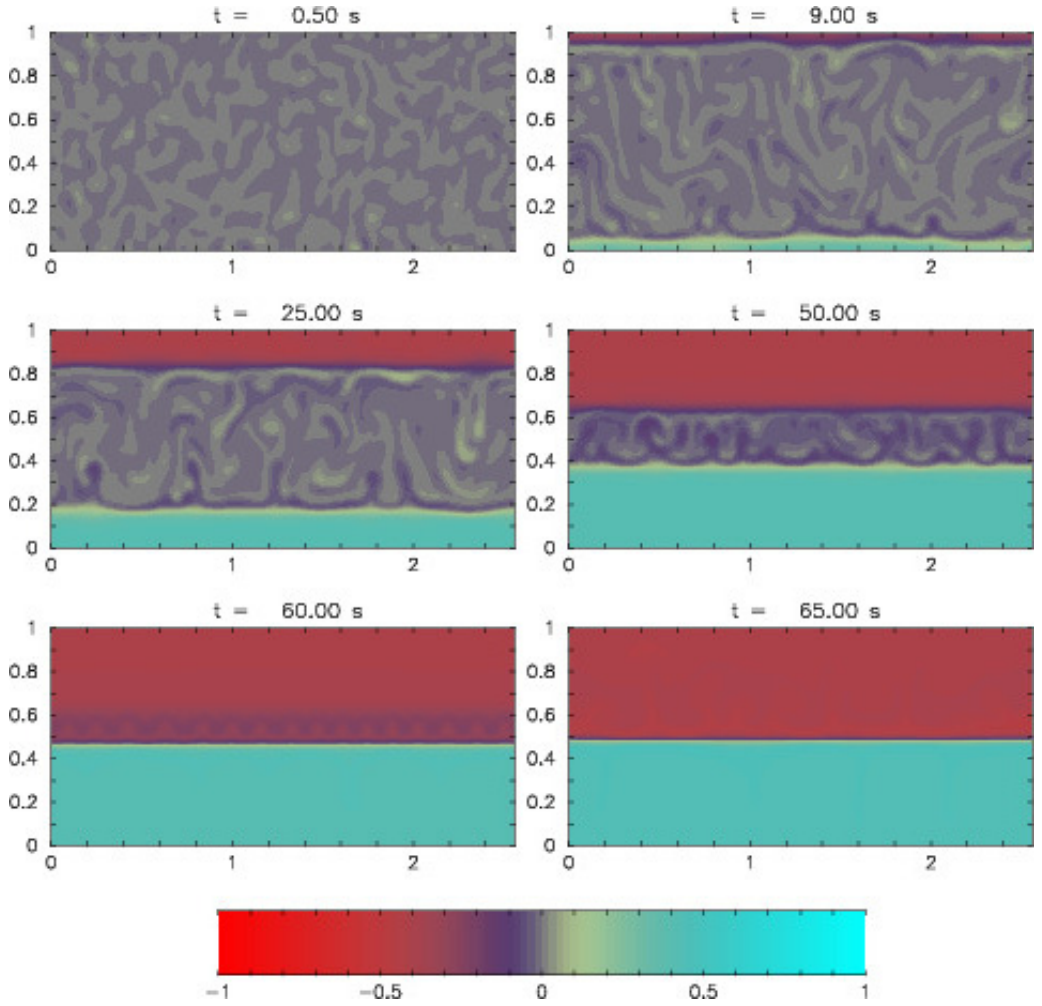

FIG. 11. Time series for $r = 0.1$, closer to the critical temperature. Due to the critical slowing down, it takes by a factor $1/r = 10$ longer until the sharp interface occurs. See the movie in the Supplemental Material [38] for time evolution of the phase field for the unforced system from a random-dot initial distribution of the phase field, closer to but below the critical temperature at $r = 0.1$.

Above T_c (when the two fluids are miscible and $r < 0$), as expected, the diffusion plays its role: The two fluids are completely mixed and there is no clear interface between them (see Fig. 12). Moreover, the value of $\varphi \to 0$ is expected in the long time limit as can also be seen in Fig. 1(a).

B. Forced system of two fluids (Faraday instability)

The previous section presented insights into the effect of phase separation dynamics when we approach the consolute temperature. In this section we subject the system to harmonic excitation to obtain Faraday instability which is investigated by DNS by solving the full nonlinear problem. The code and the parameters are the same as used before in Sec. IV A but now G is replaced by $G_e(t)$. The initial conditions correspond to a slightly disturbed flat interface, $\varphi(t = 0) = -\tanh[\frac{y-0.75}{b}] + \xi(x, y)$, with $b = 0.1$ and equally distributed numbers ξ in $[-1/4,\ 1/4]$. All the simulations have been performed with an angular frequency $\omega_0 = 100\,\mathrm{rad/s}$. The evolution is started with $a = 0$

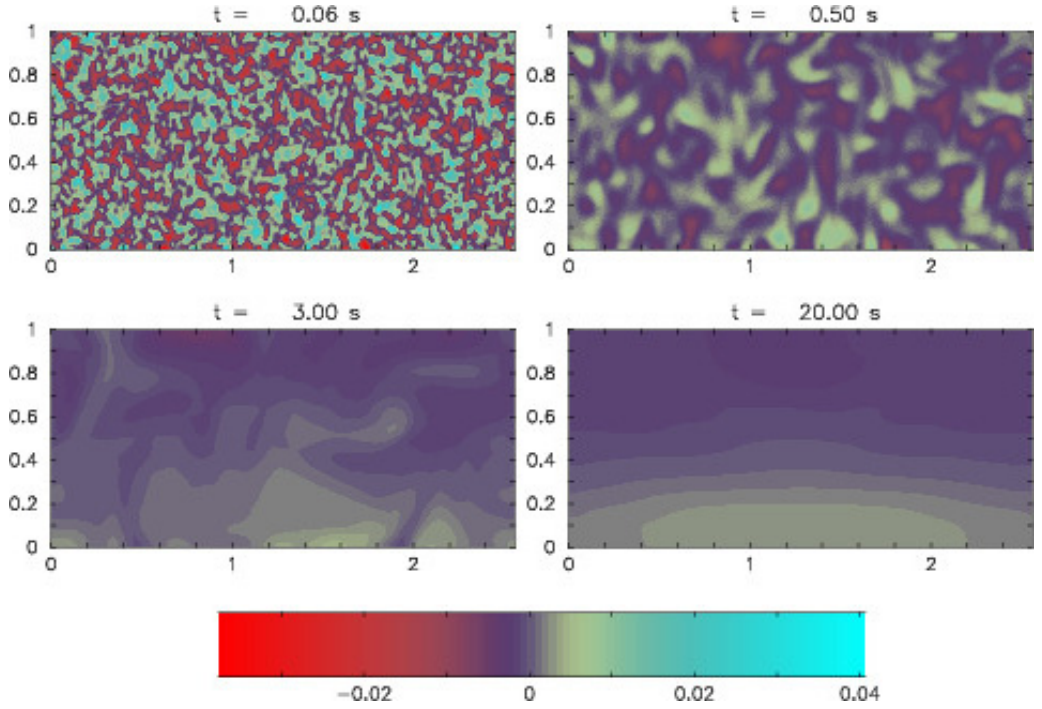

FIG. 12. Time series for $r = -0.1$, above the critical temperature. The fluids are now miscible. In the long-time limit the mixture becomes homogeneous and $\varphi \to 0$ as expected. See the movie in the Supplemental Material at [38] for time evolution of the phase field for the unforced system from a random-dot initial distribution of the phase field, above the critical temperature (miscible state) at $r = -0.1$.

up to $t = 0.1\,s$ when a sharp interface of width ζ_N has been formed. Then the vibration force is switched on with $a = 0.35$ above the critical point for $\omega_0 = 100\,\mathrm{rad/s}$; see Fig. 8. The time series is shown in Fig. 13 for $r = 1$ where after an exponentially and oscillating growth of velocity and interface deformation, the pattern oscillates subharmonically with a measured angular velocity

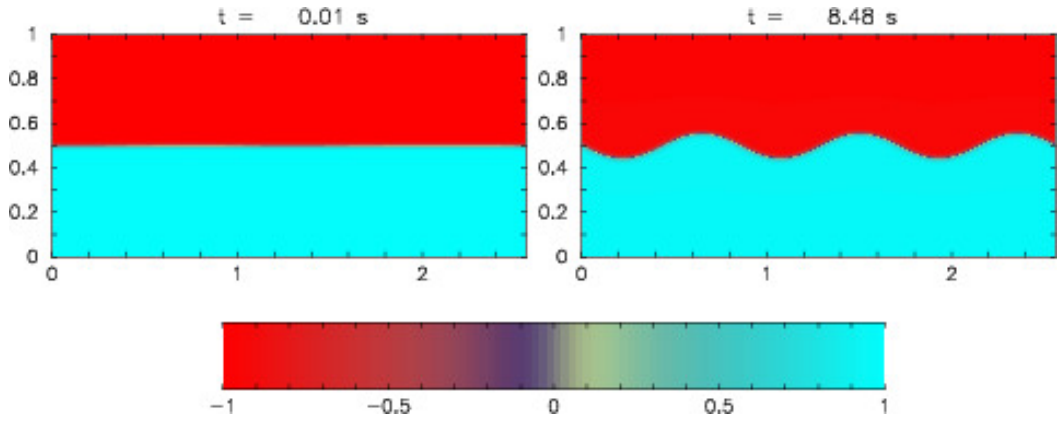

FIG. 13. Initial condition and snapshot at later time for a vibrating layer, $\omega_0 = 100$ rad/s, $a = 0.35$ above Faraday threshold and with immiscible fluids $r = 1$.

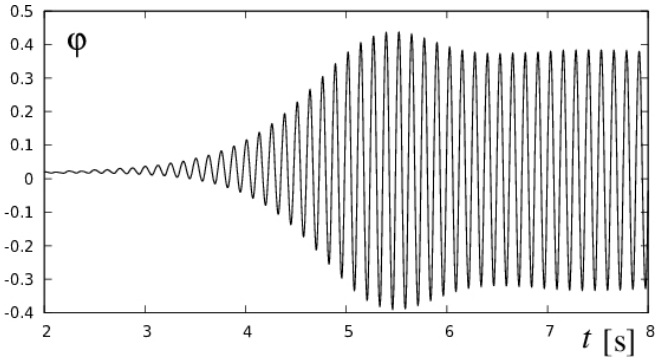

FIG. 14. Phase field at $x = 1.28\,\text{cm}$, $y = 0.5\,\text{cm}$ (middle of the layer) over time for the parameters of Fig. 13.

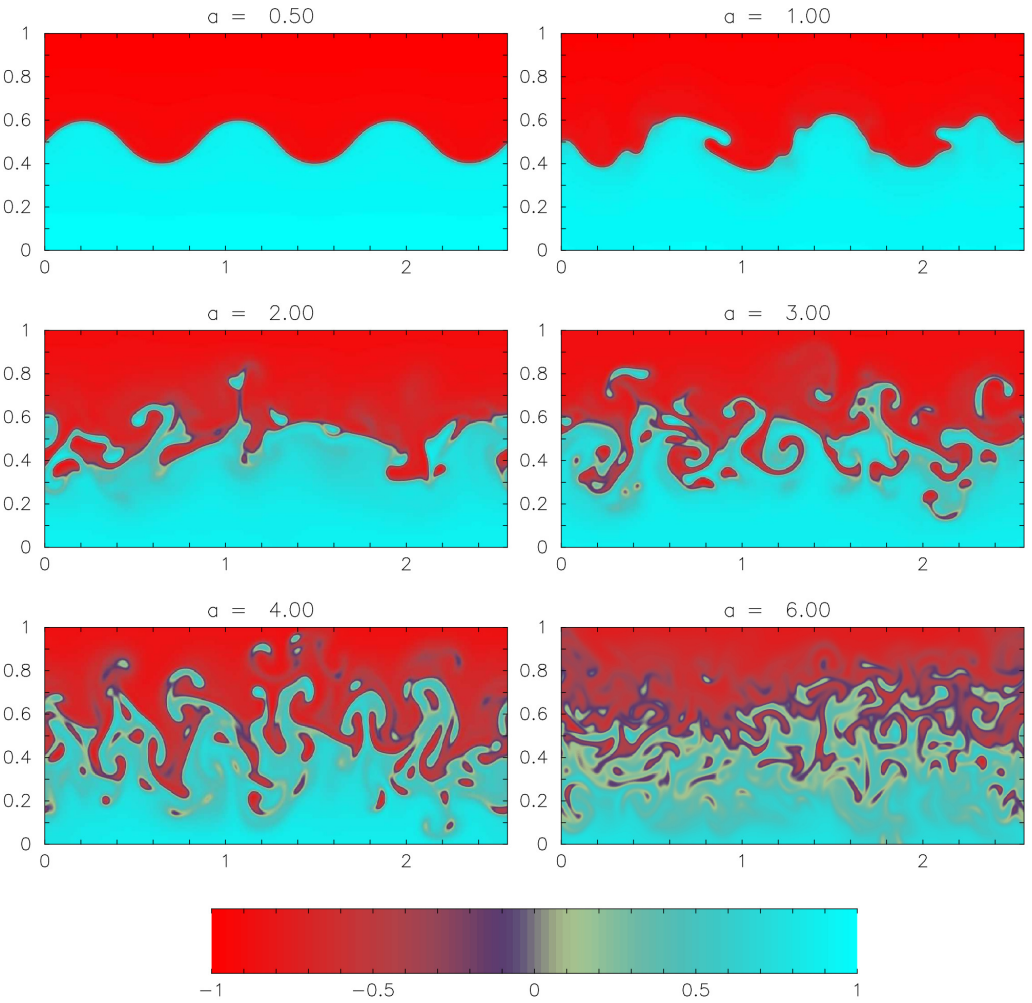

FIG. 15. Phase field contour plots for different values of acceleration parameter a which has been increased in steps after the times $t = 3.3,\ 4.0,\ 5.3,\ 5.6,\ 6.0\,\text{s}$, $r = 1$. See the movie in the Supplemental Material at [38] for time evolution of the phase field with different values of the acceleration $a = 0.5,\ 1,\ 2,\ 3,\ 4,\ 5,\ 6$ at time $t = 3.3,\ 4.0,\ 5.3,\ 5.6,\ 6.0\,\text{s}$.

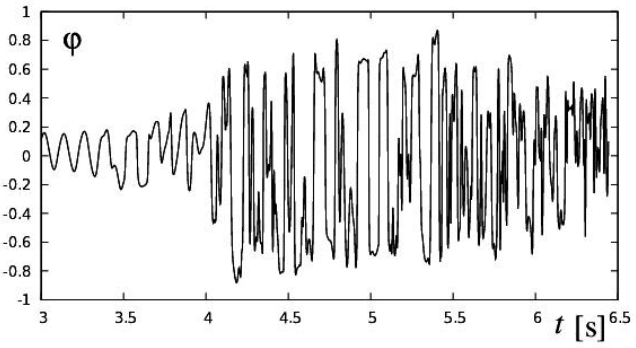

FIG. 16. Phase field at $x = 1.28$ cm, $y = 0.5$ cm (middle of the layer) over time for the case of increasing the amplitude of acceleration a as shown in Fig. 15.

of $\omega = 49.5$ rad/s, corresponding indeed to the half of the imposed frequency and showing the signature of Faraday instability (see also Fig. 14).

Figure 15 shows that if the amplitude of acceleration a is increased, patterns become more and more irregular and chaotic. After a standing wave for $a = 0.5$ (same as in Fig. 13), the interface deforms upon increasing the acceleration to $a = 1$. These deformations lead to the release of bubbles and chaotic behavior with dislocation of the interface. This chaotic behavior is clearly illustrated in Fig. 16 at one point (middle of the cavity) as a function of time.

In order to understand the effect of continuous transition we further investigate the case when we switch from the immiscible to the miscible system. Figure 17 shows the time series of the phase field for $a = 0.5$ and a case from an initial immiscible state to the miscible state. The fluid is immiscible ($r = 1$) up to $t = 5.72s$. This time represents the time when a saturated Faraday pattern is established. Then r is switched in the form of a step to $r = -0.1$, the miscible region. Pattern formation changes to smaller wavelengths and its amplitude decreases. In the long time limit, the mixture becomes homogeneous.

In Fig. 18, it is clear that when r is decreased at $t = 5.72$ s, the amplitude decreases and the interface tries to split in smaller wavelength. Then after $t \approx 8$ s, the amplitude of the oscillations decreases further and the instability terminates with the onset of diffusion causing the mixing of the two fluids. These results are in agreement with the results of linear stability analysis as presented in Fig. 6 (the wavelength decreases as we approach the critical temperature, i.e., when r decreases).

Figure 19 shows the time evolution of the phase field for $a = 0.5$ with r changing in form of a step from $r = 1$ to $r = 0.1$ after a time $t = 5.72$ s. A cascade of standing waves is found with increasing wave numbers, also in agreement with the linear results shown in Fig. 6.

Figure 20 shows the dimensionless kinetic energy over time for the sequence shown in Fig. 19, computed by averaging over space and over two periods of the external vibrations in time:

$$E_k(t) = \frac{1}{2T}\int_{t-2T}^{t} dt' \int_A \{1 + \delta\rho[\varphi(x,\, y,\, t') + 1]\}[\nabla\psi(x,\, y,\, t')]^2 dxdy,$$

with A being the dimensionless area of the layer in the xy plane. In Fig. 20, the numbers denote the number of surface waves along the interface after changing r. From the temporal behavior of E_k, one may detect how the evolution process to shorter waves takes place after decreasing r, i.e., moving closer to the critical point. As long as $r = 1$, E_k is more or less constant and three waves are seen. Then the structure rearranges itself and the mean kinetic energy decreases until five waves are selected by the system. The energy increases again but decreases thereafter when the transformation to six waves occurs. This is repeated several times until the final pattern (eight waves) stabilizes. During the whole transformation process, the amplitude of the energy decreases exponentially due to friction on the typical viscous timescale $t_\nu = d^2/\nu = 100$ s (for $d = 1$ cm). For $t \gg t_\nu$, E_k reaches

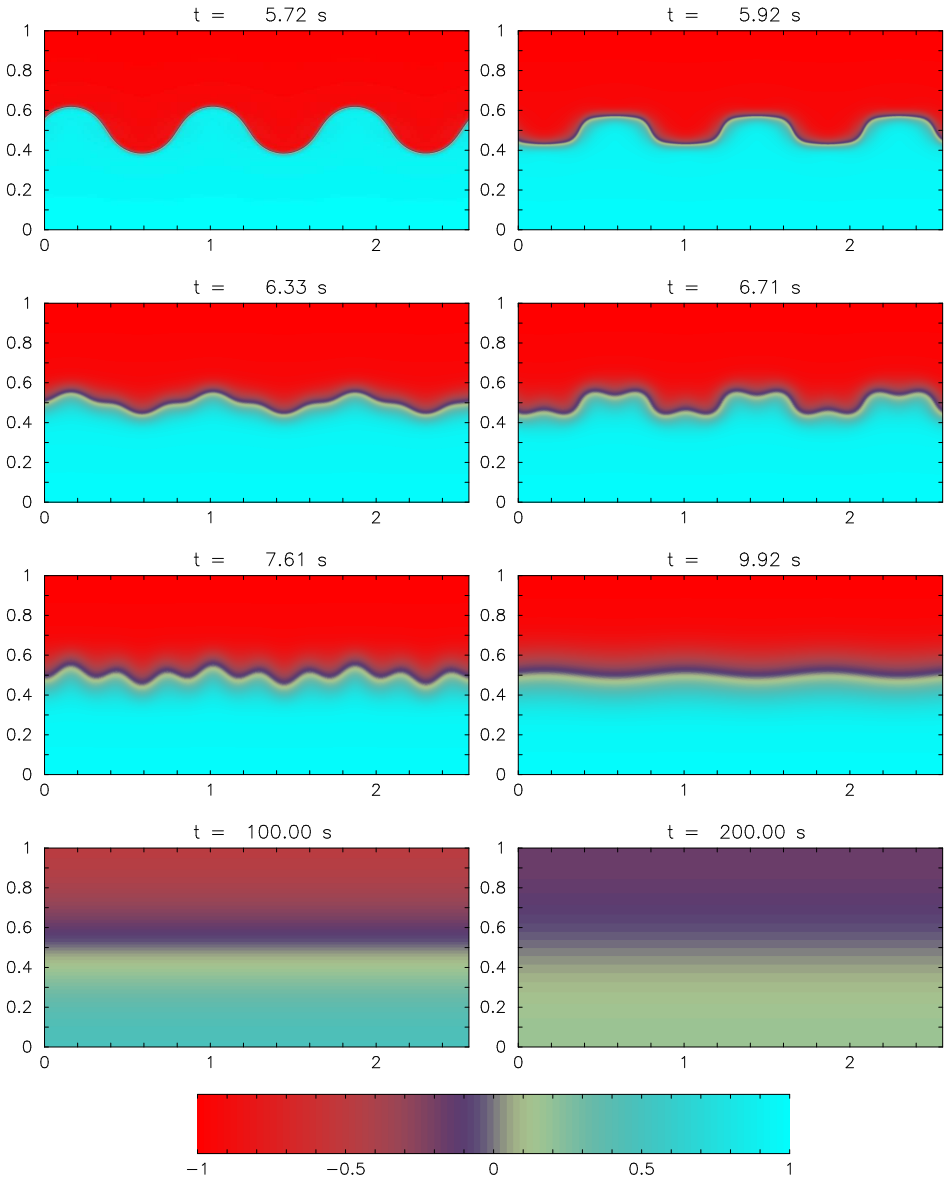

FIG. 17. Time evolution of the phase field for Faraday instability for $a = 0.5$. The fluid is immiscible ($r = 1$) up to $t = 5.72$ s; then r is switched to $r = -0.1$. See the movie in the Supplemental Material at [38] for time evolution of the phase field for Faraday instability, and time evolution from an immiscible state ($r = 1$) to a miscible state ($r = -0.1$).

asymptotically a constant finite value where the energy loss due to friction is in balance with that supplied by external forcing.

V. CONCLUSION

A phase field approach has been proposed in order to study a binary mixture evolving from an immiscible state to a miscible one. We consider the Navier-Stokes equations coupled with an

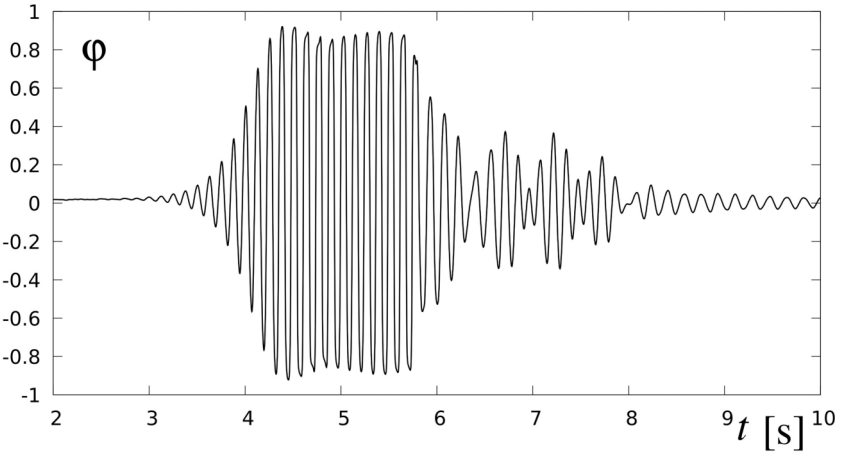

FIG. 18. Phase field at $x = 1.28\,\text{cm}$, $y = 0.5\,\text{cm}$ (middle of the layer) over time for the series of Fig. 17.

extended phase field equation through the Korteweg stresses, buoyancy, and convection terms. The free energy has been modified in order to take into account the continuous path from a phase field equation for an immiscible set of fluids to a species equation for a miscible set. For the undriven case and an immiscible set of fluids, a linear stability analysis has been performed and results from this analysis have been compared with analytical results issued from inviscid theory. We found good agreement in the frequency–wave number stability diagram with a perturbed interface which was set to an initial stable configuration. Due to external vibrations, this system can become parametrically unstable and the Faraday instability emerges. The effect of the distance to the critical temperature and the effect of the depth of the cell (or the effect of viscosity) have been adressed. Our computations showed that the wavelength decreases when the critical temperature is approached. This is also correctly reflected in the DNS with the homemade finite difference code. From these DNS results, three main results can be highlighted: (i) As the distance to the critical temperature decreases (from $r = 1$ to $r = 0.1$), the two fluids are demixed from a random initial phase field, and the one with smaller r takes much longer time for the demixing; (ii) in the case of an acceleration amplitude much larger than the critical one, the simulations show that the initial Faraday waves are split in droplets and then emerge into chaotic behavior for an acceleration as high as $6g$; (iii) when the critical point is crossed (above the critical temperature in the miscible regime), the initial Faraday standing wave is split into smaller wavelengths in concordance with the analytical results from the linear stability analysis.

A straightforward but challenging task would be to perform computer simulations for real experimental properties and parameters of the fluids and to investigate linear stability diagrams and fully nonlinear developments of the Faraday instability for different fluid viscosities and without the assumption of a Boussinesq fluid. The stability diagrams and the nonlinear solutions established in the present work will pave the way for several interesting upcoming studies.

ACKNOWLEDGMENTS

This work was partially supported by the Deutsche Forschungsgemeinschaft (DFG) under the project “Phase field modeling in phase transition problems.” It also benefited from the support of the French Space Agency (CNES) in connection with the microgravity environment.

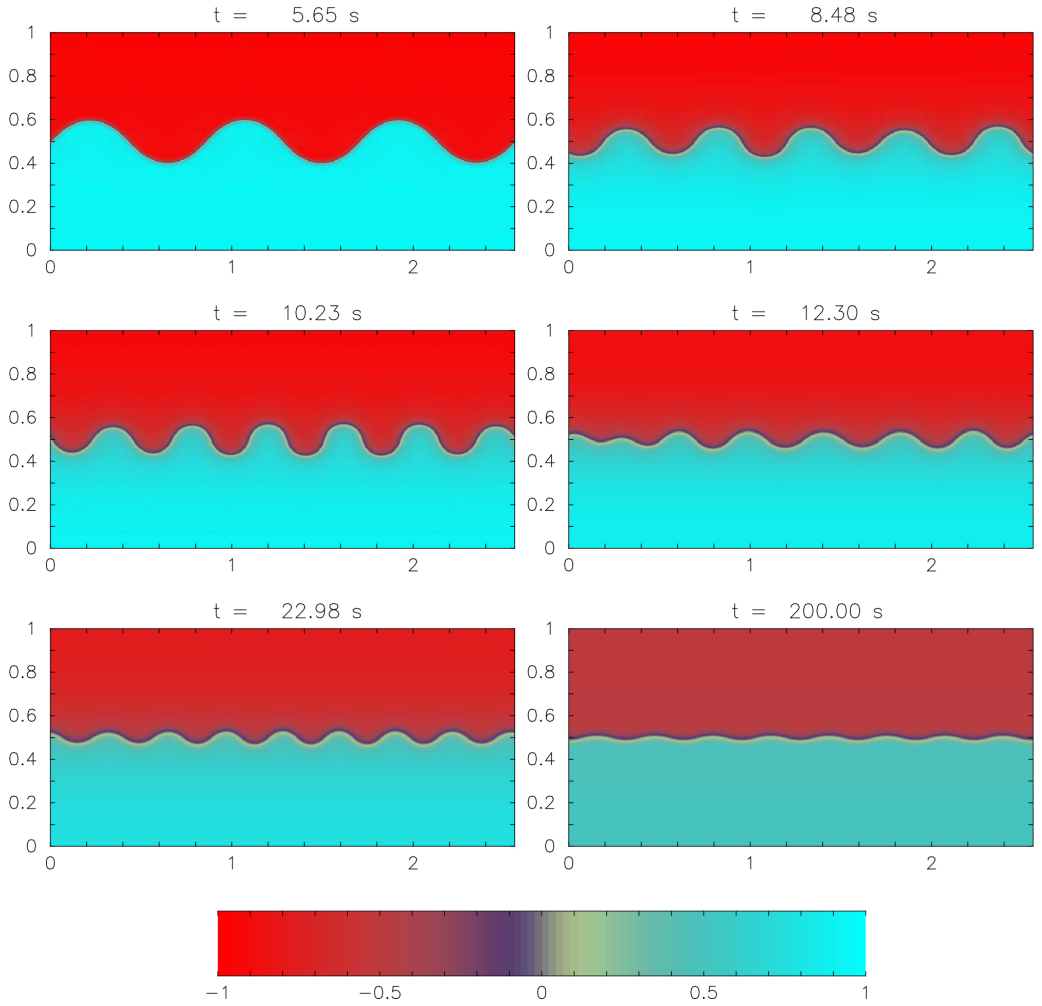

FIG. 19. Time evolution of the phase field for $a = 0.5$ with r changing from $r = 1$ to $r = 0.1$ after time $t = 5.72$ s.

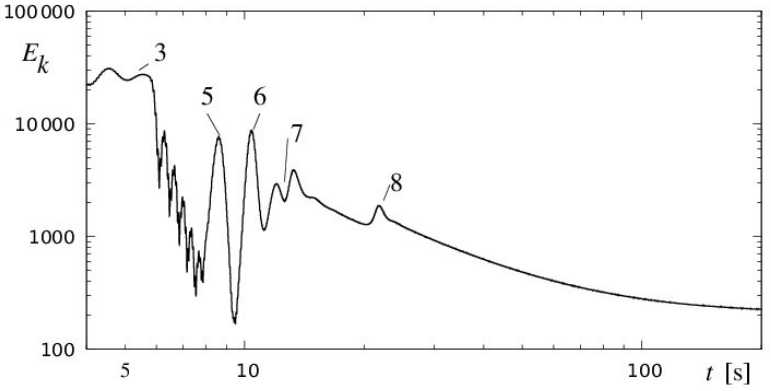

FIG. 20. Kinetic energy (dimensionless) over time for the sequence shown in Fig. 19.

APPENDIX A: STATIONARY KINK SOLUTION

For $r > 0$ a stationary solution of (2,3) gives

$$\varphi_s(y) = r^{\frac{1-q}{2}} \tanh\left[\frac{y - y_0}{\sqrt{2}\zeta}\right]. \tag{A1}$$

This corresponds to a kink located at $y = y_0$ with an interface width of

$$\zeta = \sqrt{\frac{K}{r_0}} r^{\frac{p-1}{2}}. \tag{A2}$$

The kink separates the two immiscible fluids. Here we assumed infinitely deep layers, which is a good approximation as long as ζ is much smaller than the depth of the layers.

The additional free energy per surface element compared to the uniform solution $\varphi_0 = r^{\frac{1-q}{2}}$ is equal to the surface tension of the kink and is computed from (A1) as

$$\sigma = \frac{F[\varphi_s] - F[\varphi_0]}{A} = K \int_{-\infty}^{\infty} dy \left(\frac{d\varphi_s}{dy}\right)^2 = \frac{2}{3}\sqrt{2Kr_0} r^{\frac{p+3}{2}-q}, \tag{A3}$$

where A is the surface element. From (A2) and (A3) one finds ζ_0, σ_0 as well as α, β from Sec. II C, Eq. (16).

APPENDIX B: NUMERICAL METHOD

We discretize time with the constant time step Δt as $t = n\Delta t$ and write

$$\psi(x, y, n\Delta t) \equiv \psi^{(n)}(x, y), \quad \varphi(x, y, n\Delta t) \equiv \varphi^{(n)}(x, y).$$

1. Semi-implicit time scheme

To iterate Eqs. (9) and (10) numerically, we apply a semi-implicit method in time where all linear parts of these equations, except the buoyancy term, are treated implicitly:

$$\left[\frac{1}{\Delta t} - \Delta\right]\Delta\psi^{(n+1)} = R^{(n)},$$
$$\left[\frac{1}{\Delta t} + r + \Delta - K_N\theta(r)r^p\Delta^2\right]\varphi^{(n+1)} = S^{(n)}, \tag{B1}$$

with

$$R^{(n)} = \frac{\Delta\psi^{(n)}}{\Delta t} - J(\psi^{(n)},\ \Delta\psi^{(n)}) + \delta\rho G\partial_x\varphi^{(n)} - \bar{\Gamma}_N\theta(r)r^pJ(\varphi^{(n)},\ \Delta\varphi^{(n)}),$$
$$S^{(n)} = \frac{\varphi^{(n)}}{\Delta t} - J(\psi^{(n)},\ \varphi^{(n)}) + \theta(r)r^q\Delta(\varphi^{(n)})^3, \tag{B2}$$

and the Jacobi product is defined as $J(g, h) = \partial_x g\partial_y h - \partial_y g\partial_x h$.

The functions ψ, φ, R, S are discretized in y with $y = j\Delta y$ and their derivatives are expressed by finite differences (FDs). On the right-hand sides, derivatives with respect to x were also computed with FD; for the convection terms a first-order upwind scheme is applied for stability reasons. After Fourier transforms in x for Ψ according to

$$\psi(x, y) = \frac{1}{\sqrt{2\pi}} \int dk\tilde{\psi}_j(k)e^{ikx},$$

and the same for φ, R, S, Eq. (B1) turns into a large algebraic system of the form

$$\sum_j M^{(1)}_{ij}(k)\tilde{\psi}^{(n+1)}_j(k) = \tilde{R}^{(n)}_i(k),$$
$$\sum_j M^{(2)}_{ij}(k)\tilde{\varphi}^{(n+1)}_j(k) = \tilde{S}^{(n)}_i(k), \tag{B3}$$

where $\underline{M}^{(1,2)}$ are band matrices with a bandwidth of 5 and with the elements

$$M^{(1)}_{ii} = -\frac{1}{\Delta t}(2/\Delta y^2 + k^2) - 6/\Delta y^4 - 4k^2/\Delta y^2 - k^4,$$
$$M^{(1)}_{i,i+1} = M^{(1)}_{i,i-1} = \frac{1}{\Delta t}1/\Delta y^2 + 4/\Delta y^4 + 2k^2/\Delta y^2,$$
$$M^{(1)}_{i,i+2} = M^{(1)}_{i,i-2} = -1/\Delta y^4,$$
$$M^{(2)}_{ii} = \frac{1}{\Delta t} + K_N\theta(r)r^p(6/\Delta y^4 + 4k^2/\Delta y^2 + k^4) - r(2/\Delta y^2 + k^2),$$
$$M^{(2)}_{i,i+1} = M^{(2)}_{i,i-1} = K_N\theta(r)r^p(-4/\Delta y^4 - 2k^2/\Delta y^2) - r/\Delta y^2,$$
$$M^{(2)}_{i,i+2} = M^{(2)}_{i,i-2} = K_N\theta(r)r^p/\Delta y^4.$$

2. Boundary conditions

At $y = 0,\ 1$ we assume no-slip boundary conditions, Eq. (11), and impermeability of the walls, Eq. (13).

If $\Delta y = 1/N$ with N mesh points in the y direction, the boundaries correspond to $j = 0,\ N$. The functions ψ_j and φ_j are computed only for $i = 1 \cdots N-1$ and the values at the horizontal walls follow from [Eqs. (11)–(13)]

$$\psi_0 = \psi_N = 0, \quad \varphi_0 = \varphi_1, \quad \varphi_N = \varphi_{N-1}.$$

To fulfill the two additional conditions the matrix elements for $i = 1,\ 2$ and $i = N-1,\ N$ are modified according to

$$M^{(1)}_{11} = M^{(1)}_{NN} = -\frac{1}{\Delta t}(2/\Delta y^2 + k^2) - 7/\Delta y^4 - 4k^2/\Delta y^2 - k^4,$$
$$M^{(2)}_{11} = M^{(2)}_{NN} = \frac{1}{\Delta t} + K_N\theta(r)r^p(2/\Delta y^4 + 2k^2/\Delta y^2 + k^4) - r(3/\Delta y^2 + k^2),$$
$$M^{(2)}_{12} = M^{(2)}_{21} = M^{(2)}_{N,N-1} = M^{(2)}_{N-1,N} = K_N\theta(r)r^p(-3/\Delta y^4 - 2k^2/\Delta y^2) - r/\Delta y^2.$$

3. Implementation

The equations in system (B3) are solved by a standard band system solver (LAPACK) followed by a Fourier back transform of $\tilde{\psi}^{(n+1)}_j(k)$ and $\tilde{\varphi}^{(n+1)}_j(k)$. The Fourier transforms are performed applying FFTPACK. The code is written in FORTRAN95 (Intel) and runs with double precision. The time step is restricted due to numerical instability given by the explicit terms and accuracy. In most of our runs we fixed it with $\Delta t = 1.5 \times 10^{-6}$ in dimensionless units, corresponding to $\Delta t = 1.5 \times 10^{-4}$ s. In Fig. 15 where a is rather large we used $\Delta t = 0.4 \times 10^{-6}$.

For $N = 400$ mesh points the CPU times to compute the presented series are in the range of hours on a desktop PC.

APPENDIX C: MATRIX ELEMENTS

We list the elements of the finite difference matrix $\underline{M}$ introduced in (21)

$$
\begin{aligned}
M_{11} &= -\frac{2}{\Delta y^2} - k^2 + \frac{2}{\Delta y^4} A_{11}^{-1}, \quad M_{12} = \frac{1}{\Delta y^2} + \frac{2}{\Delta y^4} A_{12}^{-1}, \\
M_{1j} &= \frac{2}{\Delta y^4} A_{1j}^{-1}, \quad j = 3 \cdots N, \quad M_{NN} = -\frac{2}{\Delta y^2} - k^2 + \frac{2}{\Delta y^4} A_{NN}^{-1}, \\
M_{N,N-1} &= \frac{1}{\Delta y^2} + \frac{2}{\Delta y^4} A_{N,N-1}^{-1}, \quad M_{Nj} = \frac{2}{\Delta y^4} A_{Nj}^{-1}, \quad j = 3 \cdots N, \\
M_{ii} &= -\frac{2}{\Delta y^2} - k^2, \quad i = 2 \cdots N-1, \\
M_{i,i-1} &= M_{i,i+1} = \frac{1}{\Delta y^2}, \quad i = 2 \cdots N-1, \\
M_{i,N+i} &= -\Gamma_N r^p k \left({\varphi_{0i}}''' + k^2 {\varphi'}_{0i} + 2 \frac{{\varphi'}_{0i}}{\Delta y^2} \right) + G \delta \rho k, \quad i = 1\, N, \\
M_{i,N+i+1} &= \Gamma_N r^p k \frac{{\varphi'}_{0i}}{\Delta y^2}, \quad i = 1 \cdots N-1, \\
M_{i,N+i-1} &= \Gamma_N r^p k \frac{{\varphi'}_{0i}}{\Delta y^2}, \quad i = 2 \cdots N, \\
M_{N+i,j} &= -k \varphi'_{0i} A_{ij}^{-1}, \quad i, j = 1 \cdots N, \\
M_{N+1,N+1} &= -\tilde{K}_N r^p \left(k^4 + \frac{4k^2}{\Delta y^2} + \frac{7}{\Delta y^4} \right) + \left(r - \varphi_{01}^2 \right) \left(k^2 + \frac{2}{\Delta y^2} \right) \\
&\quad + 3 r^q \left[2 \varphi_{01} {\varphi''}_{01} + 2 \varphi_{01}'^2 - \varphi_{01}^2 \left(k^2 + \frac{2}{\Delta y^2} \right) \right], \\
M_{2N,2N} &= -\tilde{K}_N r^p \left(k^4 + \frac{4k^2}{\Delta y^2} + \frac{7}{\Delta y^4} \right) + \left(r - \varphi_{0N}^2 \right) \left(k^2 + \frac{2}{\Delta y^2} \right) \\
&\quad + 3 r^q \left[2 \varphi_{0N} {\varphi''}_{0N} + 2 \varphi_{0N}'^2 - \varphi_{0N}^2 \left(k^2 + \frac{2}{\Delta y^2} \right) \right], \\
M_{N+i,N+i} &= -\tilde{K}_N r^p \left(k^4 + \frac{4k^2}{\Delta y^2} + \frac{6}{\Delta y^4} \right) + \left(r - \varphi_{0i}^2 \right) \left(k^2 + \frac{2}{\Delta y^2} \right) \\
&\quad + 3 r^q \left[2 \varphi_{0i} {\varphi''}_{0i} + 2 \varphi_{0i}'^2 - \varphi_{0i}^2 \left(k^2 + \frac{2}{\Delta y^2} \right) \right], \quad i = 2 \cdots N-1, \\
M_{N+i,N+i+1} &= -\tilde{K}_N r^p \left(-\frac{2k^2}{\Delta y^2} - \frac{4}{\Delta y^4} \right) - \frac{r}{\Delta y^2} + 3 r^q \left(\frac{2 \varphi_{0i} {\varphi'}_{0i}}{\Delta y} + \frac{\varphi_{0i}^2}{\Delta y^2} \right), \quad i = 1 \cdots N-1, \\
M_{N+i,N+i-1} &= -\tilde{K}_N r^p \left(-\frac{2k^2}{\Delta y^2} - \frac{4}{\Delta y^4} \right) - \frac{r}{\Delta y^2} + 3 r^q \left(-\frac{2 \varphi_{0i} {\varphi'}_{0i}}{\Delta y} + \frac{\varphi_{0i}^2}{\Delta y^2} \right), \quad i = 2 \cdots N, \\
M_{N+i,N+i+2} &= -\frac{\tilde{K}_N r^p}{\Delta y^4}, \quad i = 1 \cdots N-2, \\
M_{N+i,N+i-2} &= -\frac{\tilde{K}_N r^p}{\Delta y^4}, \quad i = 3 \cdots N.
\end{aligned}
$$

All other elements are zero. Note that due to the boundary conditions (25) the relations

$$\hat{\phi}_0 = \hat{\phi}_N = 0, \quad \hat{\phi}_{-1} = \hat{\phi}_1, \quad \hat{\phi}_{N+1} = \hat{\phi}_{N-1},$$

have been implemented.

APPENDIX D: NUMERICAL METHOD FOR FLOQUET ANALYSIS

Due to numerical stability restrictions it is important for the integration of Eq. (28) to invoke a (semi-) implicit method. We split $\underline{M}$ into

$$\underline{M}(t) = \underline{M}^{(1)} + G_e(t)\,\underline{M}^{(2)},$$

with the time-constant matrices $\underline{M}^{(1)} = \underline{M}$ with $G_e = 0$ and $M^{(2)}_{ij} = k\delta\rho\ \delta_{i,j-n}$. Now only the time-dependent part is treated explicitly, leading to the semi-implicit scheme:

$$\left(\underline{M}^{(1)} - \frac{1}{\Delta t}\underline{1}\right)\vec{Q}(t+\Delta t) = -\left[G_e(t)\underline{M}^{(2)} + \frac{1}{\Delta t}\underline{1}\right]\vec{Q}(t).$$

The advantage of the splitting method is that the matrix in the brackets on the left-hand side has to be inverted only once and not for each time step. Due to the high stability of the method, the time step is only restricted by accuracy and could be chosen quite large as $\Delta t = T_0/20$.

[1] P. Chen, Z. Luo, S. Güven, S. Tasoglu, A. V. Ganesan, A. Weng, and U. Demirci, Microscale assembly directed by liquid-based template, Adv. Mater. **26**, 5936 (2014).

[2] P. Engels, C. Atherton, and M. A. Hoefer, Observation of Faraday Waves in a Bose-Einstein Condensate, Phys. Rev. Lett. **98**, 095301 (2007).

[3] M. Faraday, On the forms and states of fluids on vibrating elastic surfaces, Philos. Trans. R. Soc. London **52**, 319 (1831).

[4] J. W. S. Rayleigh, On the crispation of fluid resting upon a vibrating support, Philos. Mag. **15**, 229 (1883).

[5] J. W. S. Rayleigh, On the maintenance of vibration by forces of double frequency and on the propagation of waves through a medium endowed with a periodic structure, Philos. Mag. **24**, 145 (1887).

[6] T. B. Benjamin and F. Ursell, The stability of a plane free surface of a liquid in vertical periodic motion, Proc. R. Soc., A **225**, 505 (1954).

[7] K. Kumar and L. Tuckerman, Parametric instability of the interface between two fluids, J. Fluid Mech. **279**, 49 (1994).

[8] M. Bestehorn, Laterally extended thin liquid films with inertia under external vibrations, Phys. Fluids **25**, 114106 (2013).

[9] M. Bestehorn and A. Pototsky, Faraday instability and nonlinear pattern formation of a two-layer system: A reduced model, Phys. Rev. Fluids **1**, 063905 (2016).

[10] S. Richter and M. Bestehorn, Direct numerical simulations of liquid films in two dimensions under horizontal and vertical external vibrations, Phys. Rev. Fluids **4**, 044004 (2019).

[11] F. Zoueshtiagh, S. Amiroudine, and R. Narayanan, Experimental and numerical study of miscible Faraday instability, J. Fluid Mech. **628**, 43 (2009).

[12] S. Amiroudine, F. Zoueshtiagh, and R. Narayanan, Mixing generated by Faraday instability between miscible liquids, Phys. Rev. E **85**, 016326 (2012).

[13] S. V. Diwakar, F. Zoueshtiagh, S. Amiroudine, and R. Narayanan, The Faraday instability in miscible fluid systems, Phys. Fluids **27**, 084111 (2015).

[14] W. Batson, F. Zoueshtiagh, and R. Narayanan, The Faraday threshold in small cylinders and the sidewall non-ideality, J. Fluid Mech. **729**, 496 (2013).

[15] J. W. Cahn and J. E. Hilliard, Free energy of a nonuniform system. I. Interfacial free energy, J. Chem. Phys. **28**, 258 (1958).

[16] J. W. Cahn and J. E. Hilliard, Free energy of a nonuniform system. III. Nucleation in a two-component incompressible fluid, J. Chem. Phys. **31**, 688 (1959).
[17] M. E. Gurtin, D. Polignone, and J. Viñals, Two-phase binary fluids and immiscible fluids described by an order parameter, Math. Models Methods Appl. Sci. **06**, 815 (1996).
[18] D. M. Anderson, G. B. McFadden, and A. A. Wheeler, Diffuse-interface methods in fluid mechanics, Annu. Rev. Fluid Mech. **30**, 139 (1998).
[19] J. Kim, Phase-field models for multi-component fluid flows, Commun. Comput. Phys. **12**, 613 (2015).
[20] H. Emmerich, Advances of and by phase-field modelling in condensed-matter physics, Adv. Phys. **57**, 1 (2008).
[21] H. Abels, H. Garacke, G. Grün, and S. Metzger, Transport processes at fluidic interfaces, *Advances in Mathematical Fluid Mechanics* (Birkhäuser, Basel, 2017).
[22] F. Magaletti, F. Picano, M. Chinappi, L. Marino, and C. M. Casciola, The sharp-interface limit of the Cahn–Hilliard/Navier–Stokes model for binary fluids, J. Fluid Mech. **714**, 95 (2013).
[23] Z. Guo and P. Lin, A thermodynamically consistent phase-field model for two-phase flows with thermo-capillary effects, J. Fluid Mech. **766**, 226 (2015).
[24] X. Xu, Y. Di, and H. Yu, Sharp-interface limits of a phase-field model with a generalized Navier slip boundary condition for moving contact lines, J. Fluid Mech. **849**, 805 (2018).
[25] S. Mirjalili, C. B. Ivey, and A. Mani, A conservative diffuse interface method for two-phase flows with provable boundedness properties, J. Comput. Phys. **401**, 109006 (2020).
[26] D. Jacqmin, Calculation of two-phase Navier-Stokes flows using phase-field modeling, J. Comput. Phys. **155**, 96 (1999).
[27] H. Ding, P. D. M. Spelt, and C. Shu, Diffuse interface model for incompressible two-phase flows with large density ratios, J. Comput. Phys. **226**, 2078 (2007).
[28] D. Jasnow and J. Vinals, Coarse-grained description of thermo-capillary flow, Phys. Fluids **8**, 660 (1996).
[29] J. Lowengrub and L. Truskinovsky, Quasi-incompressible Cahn–Hilliard fluids and topological transitions, Proc. R. Soc. London, Ser. A **454**, 2617 (1998).
[30] K. Takagi and T. Matsumoto, Numerical simulation of two-dimensional Faraday waves with phase-field modelling, J. Fluid Mech. **686**, 409 (2011).
[31] U. Thiele, S. Madruga, and L. Frastia, Decomposition driven interface evolution for layers of binary mixtures. I. Model derivation and stratified base states, Phys. Fluids **19**, 122106 (2007).
[32] V. Jajoo, Faraday instability in binary fluids, Ph.D. thesis, University of Bordeaux, 2017, available online at https://tel.archives-ouvertes.fr/tel-01695491.
[33] R. Borcia and M. Bestehorn, Phase-field model for Marangoni convection in liquid-gas systems with a deformable interface, Phys. Rev. E **67**, 066307 (2003).
[34] R. Borcia, D. Merkt, and M. Bestehorn, A phase-field description of surface-tension-driven instability, Int. J. Bifurcation Chaos **14**, 4105 (2004).
[35] M. Bestehorn, *Computational Physics* (De Gruyter, Berlin, 2018).
[36] C. A. J. Fletcher, *Computational Techniques for Fluid Dynamics* (Springer, Berlin, 2013), Vol. 2.
[37] S. Chandrasekhar, *Hydrodynamic and Hydromagnetic Stability* (Dover, NewYork, 1961), p. 428ff.
[38] See Supplemental Material at http://link.aps.org/supplemental/10.1103/PhysRevFluids.6.064002 for the movies related to Figures 9, 10, 11, 12, 15 and 17.